Bi^{3+} doping in 1D $((CH_3)_3SO)PbI_3$ pseudo-perovskites: a realistic model for defect interactions in optoelectronic materials

Candida Pipitone,[1,] Silvia Carlotto,[2] Maurizio Casarin,[2] Alessandro Longo,[3,4] Antonino Martorana,[1] Francesco Giannici[1,*]*

[1] Dipartimento di Fisica e Chimica "Emilio Segrè", Università di Palermo, viale delle Scienze, I-90128 Palermo, Italy

[2] Dipartimento di Scienze Chimiche, Università di Padova and Institute of Condensed Matter Chemistry and Technologies for Energy (ICMATE), National Research Council (CNR), via Marzolo 1, I-35131 Padova, Italy

[3] ESRF - The European Synchrotron, CS 40220, 38043 Grenoble Cedex 9, France

[4] Istituto per lo Studio dei Materiali Nanostrutturati, Consiglio Nazionale delle Ricerche, Via Ugo La Malfa 153, 90146 Palermo, Italy

** to whom correspondence should be addressed: candida.pipitone@unipa.it and francesco.giannici@unipa.it*

Abstract

The recently described monodimensional hybrid pseudo-perovskites $((CH_3)_3SO)PbI_3$ exhibits complete Pb^{2+}/Bi^{3+} miscibility in the B site. Heterovalent substitution imposes that charge-compensating defects are introduced in the lattice as well. This paper reports the energetics of point defects and the interaction between charge-compensating defects that occur upon Bi^{3+} doping in $((CH_3)_3SO)PbI_3$. Periodic DFT simulations were employed to analyze the formation energy of Pb^{2+} vacancies, $(CH_3)_3SO^+$ vacancies, iodide vacancies, or the insertion of interstitial iodide ions.

Solid solutions with a large Bi^{3+} content were modeled considering different charge compensation defects (Pb^{2+} vacancies, $(CH_3)_3SO^+$ vacancies, and interstitial iodide) to consider electrical neutrality. Both the formation energy evaluation and the structural parameters after relaxation are in very good agreement with available experimental data (both X-ray diffraction and absorption spectroscopy), confirming that Pb^{2+} vacancies are indeed the primary ionic charge-compensation mechanism leading to

solid solutions described by the formula $((CH_3)_3SO)_3Pb_{3x}Bi_{2(1-x)}V_{(1-x)}I_9$ $(0 < x < 1)$, where V indicates a B site vacancy. As a consequence of the complete miscibility, the defect concentration at intermediate compositions is considerable, and it is probably responsible for various peculiar structural effects observed, e.g., in $((CH_3)_3SO)_3Pb_{0.99}Bi_{1.34}I_9$, which are related to short-range order phenomena in the chain composition.

Atomistic simulations were then carried out to estimate defect-defect interactions as a function of their respective positions inside the linear PbI_6/BiI_6 octahedral chains. The resulting bond energies for atom pairs and triads effectively explain the relative stability of defect clusters. This approach is expected to shed light on the short-range order in this class of doped materials, but it can be extended to other structures as well. The understanding of defect structures, and control of structural and electronic properties, have implications for the engineering of doped materials, which find vast applications in optoelectronic devices.

Keywords: hybrid lead-bismuth halides, trimethylsulfoxonium, DFT, solid solution, ionic defectivity, formation energy.

1. Introduction

Properties engineering of existing materials is at the forefront of hybrid halide perovskites research. Even if this class of compounds has been the subject of many experimental and theoretical studies in the last decade for energy applications such as photovoltaics, thermoelectrics, laser, and detector devices, the achieved performances are still not adequate for large-scale use.[1,2] Among the functional properties that need to be modulated to enhance the performance, the most important are chemical and thermal stability, optical bandgap, and carrier mobility. All of them can be considerably modified by reducing the connectivity of the inorganic scaffold[3–5]: the three-dimensional ABX_3 perovskite framework composed of corner-sharing $[BX_6]$ octahedra can be broken down into one, two, or three dimensions, resulting in the 2D, 1D, or 0D lower-dimensional structures respectively (more properly described as pseudo-perovskites).[6] These materials are appealing due to their unique

characteristics: generally chemically stable to air and moisture, unlike 3D hybrid halides, and exhibit unprecedented tunability in the electronic structure. However, they often feature wide band gaps and low charge concentration, mobility, or both: all of which are undesirable for applications. Due to the high structural flexibility and defect tolerance of these compounds, compositional engineering is a powerful tool to overcome the actual shortcomings of pseudo-perovskites. The presence of any kind of impurity (e.g., intrinsic defects and dopant atoms) into a periodic lattice is bound to influence the performance of a perovskite-based device. The intentional introduction of dopants is usually aimed to enhance the charge transport properties of the pristine compound. It can also introduce intrinsic or charge-compensating defects that can severely limit the efficiency of optoelectronic devices by acting as carriers recombination centers. [7,8] Since countless combinations of (multiple) dopants in different lattice sites could in principle be considered, ab initio modelization methods of such systems are of fundamental importance to direct the experimental efforts in the right direction. [7] To date, most theoretical studies have been devoted to the study of homovalent doping in 3D perovskites. Heterovalent doping has remained relatively less studied until recently due to the complexity of the charge compensation mechanisms that must be considered. In particular, bismuth has been investigated as a donor dopant for various inorganic and hybrid 3D perovskites [9–16].

Bi^{3+} doping in 3D perovskites (most notably, methylammonium lead iodide or bromide – MAPI or MAPBr) is a debated topic, since the experimentally determined charge carrier concentration is orders of magnitude lower than expected from Bi donor concentration. Rakita et al. [15] examined several possible causes for this behavior, including the formation of stable defect pairs, or thermodynamic and kinetic instability of the defects. An interpretation of the lattice parameter changes in MAPI after Bi doping has been proposed very recently, using elastic properties of the bulk and DFT simulations. Different point defects compensating for Bi^{3+} are possible, whose nature is, however, still unclear. [13] In MAPI, most studies attribute the formation of deep traps to Bi^{3+} doping, hindering electron transport [14,16]; it was also proposed that the Bi donors shift the Fermi level instead, causing, in turn, an increased concentration of I-interstitials. [10] A careful control of the synthetic conditions was therefore proposed to balance the opposing tendencies towards I-vacancy and I-interstitial formation. In the

following, we also discuss the effect of the iodine chemical potential on the formation energy of the various point defects. In any case, the metal site doping of pseudo-perovskites with lower connectivity remains nearly unexplored both experimentally and theoretically. Their substantially higher stability than 3D structures opens new possibilities to achieve extremely high defect concentrations in bulk, kinetically, and/or thermodynamically stabilized. [15]

In this work, we carried out a periodic ab initio study of the energetics of heterovalent Bi^{3+} doping and defect creation in a trimethylsulfoxonium (TMSO) 1D pseudo perovskite $(TMSO)PbI_3$. The presence of sulfur-based aprotic cations leads to lower-dimensional, highly air-stable compounds. The alkylammonium cations, on the contrary, result in highly hygroscopic hybrid compounds, vulnerable to moisture degradation [17]. For instance, the use of $TMSOPbI_3$ in 1D/3D photovoltaic devices employing $CH_3NH_3PbI_3$ has been recently reported to lead to increased performance and moisture resistance. [18] We recently described the crystal structure and phase diagram of the $(TMSO)PbX_3/(TMSO)_3Bi_2X_9$ system with X=(I, Br), reporting complete miscibility of Pb^{2+}/Bi^{3+} in the B-site throughout the composition range. [19] This work explores the defect formation mechanisms needed to compensate for the difference in charge between lead and bismuth. Our simulations show that the formation of Pb^{2+} vacancies for each two Bi^{3+} dopant atoms is the most probable mechanism, confirming the previous assumption from XRD data. The electronic band structure of the Bi-doped compounds shows the presence of deep trap defect states in the bandgap below the conduction band. The different possible configurations for the dopant and defects among chains are also considered to evaluate the interaction between adjacent B sites in the structure. These interactions are bound to affect the optoelectronic properties of the doped materials and their bandgap.

While the insertion of Bi^{3+} cations in the perovskite B-site gives rise to a single-phase roughly following the Vegard law, very peculiar X-ray powder diffraction peak shapes are observed at higher Bi content hinting at significant short-range order, driven by first neighbor interactions between B-sites [19]. Atomistic simulations were therefore carried out to study the energetics of different defect configurations in highly defective supercells. Accordingly, this study enables to bridge the gap between the short-order phenomena and functional properties of $((CH_3)_3SO)_3Pb_{3x}Bi_{2(1-x)}V_{(1-x)}I_9$ $(0 < x < 1)$ solid

solutions, providing a precious tool to guide in the development of better performing hybrid pseudo-perovskites for green energies applications.

2. Methods

Periodic ab initio quantum mechanical calculations were carried out with density functional theory (DFT) using the PWscf package in the Quantum Espresso suite [20–22]. Kohn–Sham equations are solved with the generalized gradient approximation (GGA) [23], adopting the PBE exchange-correlation functional [24] within the Projector Augmented Wave method (PAW) [25], with an energy cutoff of 50 Ry.

A TMSOPbI_3 2x1x1 supercell containing 144 atoms was fully relaxed and used as a starting point for further calculations. All structure relaxations and single-point calculations were carried out on centered 2 x 2 x 2 and 4 x 4 x 4 Monkhorst-Pack (MP) grids, respectively. The spin-orbit coupling (SOC) was considered for the lead, bismuth, and iodide atoms in the band structure calculations. The convergence threshold criteria are as follows: 10^{-6} a.u. for electronic structure, 10^{-4} a.u. on total energy, 10^{-2} a.u. on forces, and 0.5 kbar on the pressure, respectively.

The energy of charged defects in supercells was corrected using the correction schemes implemented in the program CoFFEE: Corrections For Formation Energy and Eigenvalues [26].

$(TMSO)_3Pb_{0.99}Bi_{1.34}I_9$ was prepared as described in ref. 19. The extended X-ray absorption fine structure (EXAFS) spectra were acquired at beamline LISA of the ESRF and analyzed with Viper [27].

3. Results and discussion

3.1. Undoped (TMSO)PbI_3

(TMSO)PbI_3 crystallizes in the orthorhombic *Pnma* space group (Figure 1a). Each Pb^{2+} cation is octahedrally coordinated to six iodide anions [PbI_6]. The octahedra are connected throughout faces, with each iodide bound to two lead cations with Pb-I distances between 3.16 and 3.26 Å. The resulting infinite $[PbI_3]_\infty$ polyanionic chains form the framework of a one-dimensional structure. The chains run parallel to the *a*-

axis, so the Pb-Pb distance (3.91 Å) corresponds to half of the ***a*** lattice parameter (7.82 Å). The $[PbI_3]_\infty$ chains are interspersed with TMSO cations, leading to a 1D pseudo-perovskite structure. The supercell approach was then used to calculate the formation energy of point defects. The unit cell contains four $TMSOPbI_3$ formula units, so the content of the undefective unit cell is described as $(TMSO)_4Pb_4I_{12}$, where the four Pb^{2+} ions reside in two parallel linear chains. Due to its size, the crystallographic structure was replicated along the **a** direction (i.e., the short axis), leading to a $(TMSO)_8Pb_8I_{24}$ 2x1x1 supercell (Figure 1b). The **a** direction choice leads to two linear chains containing four Pb^{2+} sites each. Structural relaxation of this supercell (a = 15.66 Å, b = 11.57 Å, and c = 14.72 Å) results in a slightly larger volume than the experimental one (+0.16%, +3.35%, and +2.36% on each axis, respectively). The optimized supercell structure is used as a reference for all calculations hereafter.

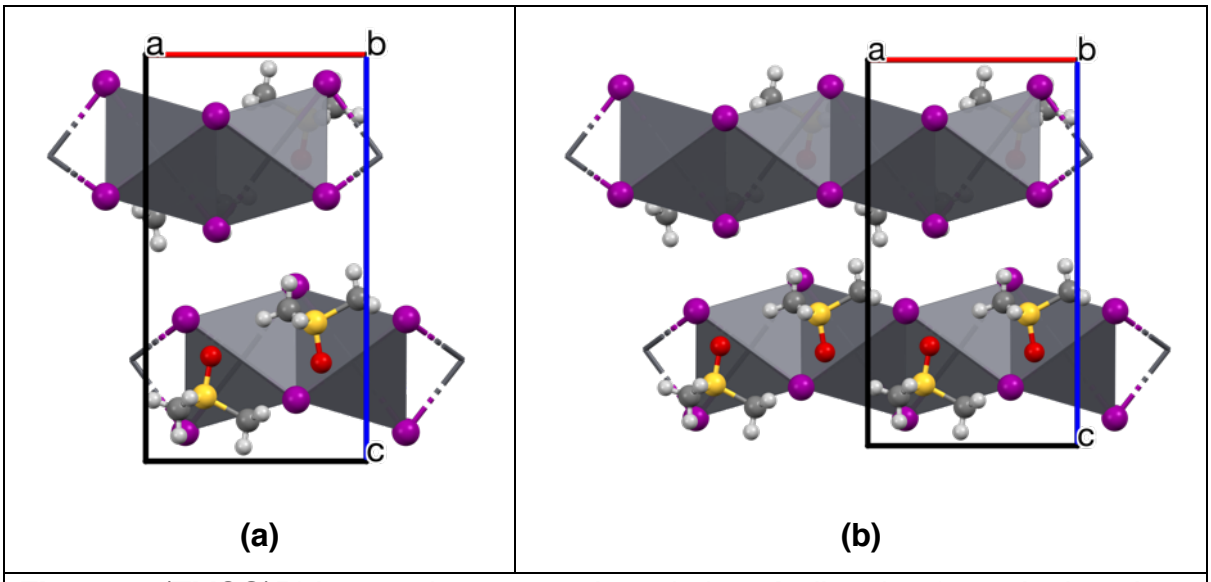

Figure 1. $(TMSO)PbI_3$ crystal structure viewed along **b** direction for a single unit cell (a) and repetition of two unit cells along a direction (b). Iodine atoms in violet, PbI_6 octahedra in grey. Carbon, sulfur, oxygen, and hydrogen atoms in grey, yellow, red, and white, respectively.

3.2 Point defects in the dilute limit

To investigate the relative stability of defects in $(TMSO)PbI_3$ lattice, the choice of the chemical potential is essential to calculate the defect formation energy. Indeed, it must assure the stability of the perovskite against precipitation of elemental phases (e.g.,

metallic Pb) and secondary phases (e.g., PbI_2), leading to boundary conditions that define acceptable ranges for chemical potentials (see Supporting Information). In the following, the chemical potential of element X (μ_X) is chosen with respect to the standard chemical potential as $\mu_X = \Delta\mu_X + \mu_X^\circ$. The μ_X° values are calculated from elemental phases.

These boundary conditions can be partially represented graphically in a phase diagram. We evaluate the relative stability of defects in three different conditions inside the $(TMSO)PbI_3$ stability regions (Figure S1): these are Bi-rich (1), Pb-rich (2), and I-rich conditions (3), respectively.

The formation energy of a defect in a semiconductor is expressed as Eq. 1 [28] :

$$E_{form} = E_{defect} - E_{pristine} - \sum n\,\mu_X + q\,(E_{VBM} + E_F) + q\,E_{corr} \qquad \textit{(Eq. 1)}$$

Where E_{defect} and $E_{pristine}$ are the total energy of the defective and undefective supercells, respectively; *n* is the number of atoms introduced or removed from the pristine supercell; μ_X is the chemical potential of the exchanged element; *q* is the defect charge; E_F is the Fermi level (chemical potential of electrons) relative to the energy maximum of the valence band E_{VBM}. The E_{corr} term represents the correction for the electrostatic interaction of a charged defect with its periodic images.

Various strategies to correct the formation energy of charged defects have been developed in the last two decades and extensively tested on simple semiconductors [29–31], and their shortcomings were critically examined by Castleton et al. [32].

The formation energies of point defects are shown in Figure 2. For each point defect, the most stable charge state is shown as a function of the Fermi level, and the charge reflects on the slope of E_{form}.

The iodine vacancy turns out to be the most energetically favorable intrinsic defect in almost any condition. The formation of iodine vacancies has been recently proved to enhance the ionic conductivity of $(CH_3NH_3)PbI_3$ under illumination. [33] The enhancement is driven by defect-mediated ion migration: this kind of effect can be beneficial for solar cell efficiency [34–36]. It could also affect the conductivity in thermoelectric applications, where poor electrical transport is a significant issue in pseudo-perovskites.

All the charge level transitions within the defect (e.g., from V_{TMSO}^{x} to $V_{TMSO}^{\prime}$), whose energy is independent on μ_X, are reported in Figure 3a. While V_I and Bi_{Pb} don't present charge transition within the bandgap, V_{Pb} and V_{TMSO} are deep donors with charge transition in the upper half of the bandgap. Thus they can be a primary source of charge trapping. Iodine interstitials, on the contrary, are shallow donors with charge transition near the conduction band. Nevertheless, even if these defects can trap and scatter charge carriers, their formation energy is relatively high in all the selected conditions, and therefore unlikely to be found in appreciable concentrations. The lowest-energy donor-acceptor defects couples (e.g., from $Bi_{Pb}^{\bullet}$ to V_{TMSO}^{x}) can pin the Fermi level: the position of each couple under the different chemical potential conditions is illustrated in Figure 3b. All the synthetic conditions chosen tune the Fermi level towards *n-type* semiconductors. Moreover, in excess of iodine, all the donor-acceptor pairs lie immediately below the CBM, creating several near states that can more easily de-trap charges and help in carrier transport.

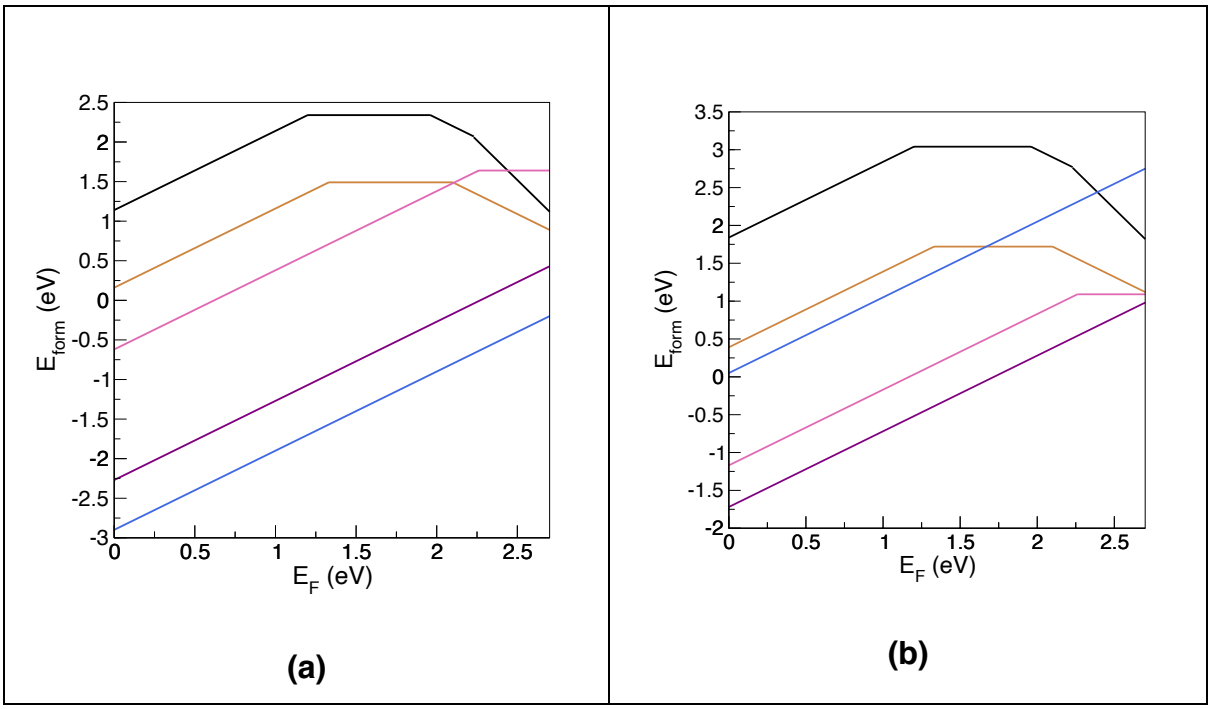

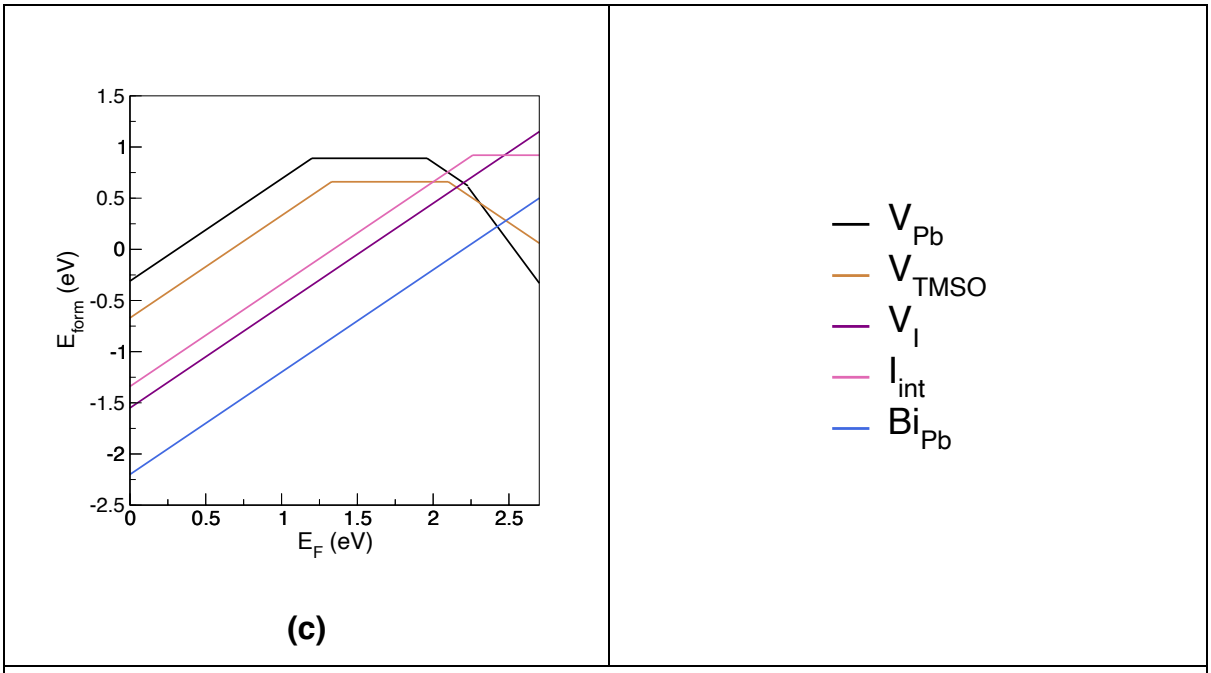

Figure 2. The formation energy of point defects in (TMSO)PbI_3 as a function of the Fermi level relative to VBM, for Bi-rich (a), Pb-rich (b), and I-rich (c) conditions.

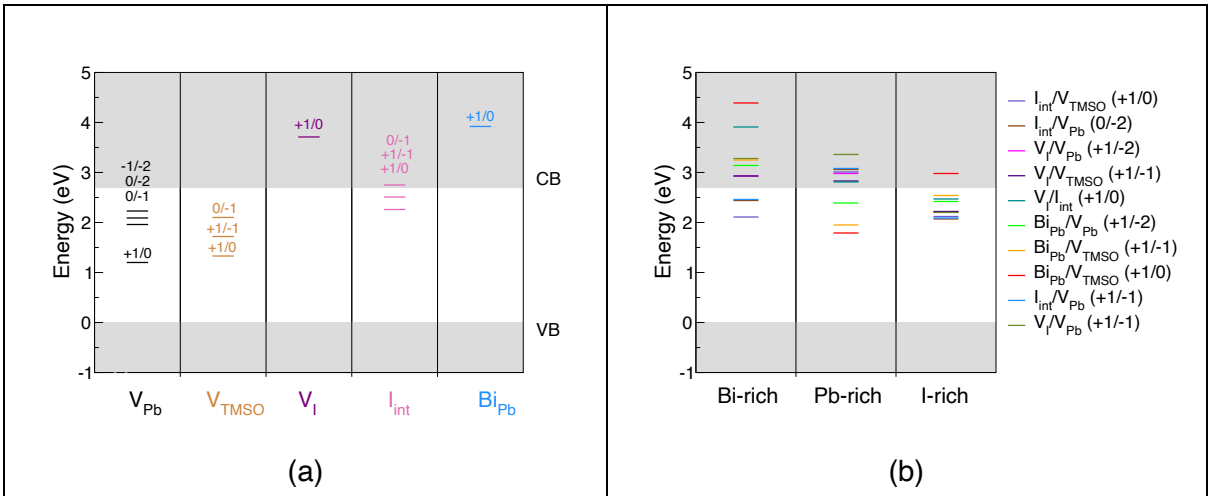

Figure 3. (a) Charge level transitions of defects. (b) Donor-acceptor defects (with charges) in the different chemical potential conditions.

3.3. $Bi_{Pb}^{\bullet}$ defects and the charge compensation mechanisms

Upon bismuth doping, it is expected that the Bi^{3+} cation substitutes Pb^{2+} forming a $Bi_{Pb}^{\bullet}$ defect. While the rare +5 oxidation state may exist for bismuth in some oxides, only the +3 state has been reported so far in its chlorides, bromides, and iodides. [37] The difference in charge between the two cations invokes a charge compensation mechanism to preserve electroneutrality. For this reason, either vacancies or

interstitials (*ionic compensation*) or electrons or holes (*electronic compensation*) defects must also be introduced. The former is known to be more likely to happen for this kind of hybrid structure [38], thus in this work, three possible mechanisms involving ionic compensation with negatively charged defects were considered, described by the following Kröger-Vink equations:

(i) Lead vacancy: V''_{Pb}

$$3\,Pb^{x}_{Pb} + 2\,BiI_3 \rightarrow 2\,Bi^{\bullet}_{Pb} + V''_{Pb} + 3\,PbI_2 \qquad \text{(Eq. 2)}$$

(ii) TMSO vacancy: V'_{TMSO}

$$TMSO^{x}_{TMSO} + Pb^{x}_{Pb} + BiI_3 \rightarrow Bi^{\bullet}_{Pb} + V'_{TMSO} + PbI_2 + (TMSO)I \qquad \text{(Eq. 3)}$$

(iii) I interstitial: I'_i

$$Pb^{x}_{Pb} + BiI_3 \rightarrow Bi^{\bullet}_{Pb} + I'_i + PbI_2 \qquad \text{(Eq. 4)}$$

The above mechanisms (depicted in Figure 4) involve forming a negative defect to compensate for the positively charged Bi^{3+} dopant. As a consequence, neutral defect complexes are formed overall. In particular, the mechanism (i) was previously assumed - from stereochemical considerations - to be the primary charge compensation mechanism. [19] To corroborate this hypothesis and evaluate the possibility of coexisting charge compensation mechanisms, a computational study on the energy formation and the geometrical parameters for these defects complexes is carried out in the following.

3.4. Ionic compensation mechanisms: E_b and structure parameters

Bi-doped $TMSOPbI_3$ is best described as a continuous solid solution between $TMSOPbI_3$ and $(TMSO)_3Bi_2I_9$ [19]. In this respect, the supercells described below are realistic descriptions of the structure and composition of the doped compounds at

various Bi levels between 12% and 67%. This means that there are no spurious interactions between periodic images of the defects to be taken into account.

For mechanism *(i)*, introducing two bismuth atoms and one vacancy in the 8 B sites of the pristine supercell ($TMSO_8Pb_8I_{24}$) results in a $TMSO_8Pb_5Bi_2I_{24}$ composition (28.6% doping level). A higher doping level is also possible within the same supercell for this mechanism: the substitution of six Pb^{2+} by four Bi^{3+} and two vacancies, resulting in $TMSO_8Pb_2Bi_4I_{24}$ (66.7 Bi%). Since the experimental evidence shows the formation of a single-phase throughout the phase diagram (from 0 to 100% Bi),[19] both dopant percentages were considered. With the same fashion, the two lowest possible doping levels for the the mechanisms *(ii)* and *(iii)* have been investigated leading to composition described by $TMSO_7Pb_7BiI_{24}$ (Bi=12.5%) and $TMSO_6Pb_6Bi_2I_{24}$ (Bi=25%) for the TMSO vacancy, and $TMSO_8Pb_7BiI_{25}$ (Bi=12.5%) and $TMSO_8Pb_6Bi_2I_{26}$ (Bi=25%) for the interstitial iodide. As two or three defects are contemporary present in the cell, several different configurations arise, depending on the position of the defects with respect to each other. For simplicity, just one configuration for *(i)*, *(ii)*, and *(iii)* has been considered. In each case, placed the charge compensation defect (V_{Pb}, V_{TMSO}, or I_i), all the different configurations has been evaluated by placing the Bi_{Pb} defect in each of the possible different sites. Among all possible defect configurations, it is found that the lowest energy configurations for each mechanism are those where the bismuth atom(s) and the compensating defect(s) are as close as possible, and they were then used for further calculation.

The binding energy (E_b) of each neutral defect complex is calculated as:

$$E_b(X+Y) = E_{form}(X+Y) - E_{form}(X) - E_{form}(Y) \qquad (Eq.\ 5)$$

Where E_{form} is the formation energy of the defect in its neutral charge state. The formation energies for the defects described in Eqs. 2-4 are calculated as described in paragraph 3.2. The binding energy values obtained are reported in Table 1. All the neutral defect complexes show negative binding energy, which indicates a high probability of formation of defect complexes compared to individual defects. Among the three possible mechanisms, the one involving V''_{Pb} (mechanism *(i)*) is much more favored, with markedly lower bonding energy (-4.62 eV) than the others (-2.17 and -

1.35 eV). These outcomes confirm Eq. 2, the lead vacancy, as the major compensation mechanism for the $(TMSO)PbI_3$ - $(TMSO)_3Bi_2I_9$ solid solutions.

Further evidence for mechanism (*i*) comes from comparing the geometrical parameters (both cell parameters and bond distances) of the relaxed structures and the experimental data. The cell parameters of the relaxed cells were also compared to the experimental trend reported recently [19]. The experimental X-ray diffraction data acquired over the whole Pb/Bi composition range show a significant contraction of only **a** lattice parameter (i.e., the direction along which the chains are oriented). In contrast, the *b* and *c* parameters (normal to the chains) remain unchanged upon doping. These trends of **a**, **b**, **c,** and **V** parameters against the %Bi of the experimental data are reported in Figure 5 and compared to the one obtained from the relaxation of the supercell herein described. As expected, the mechanism *(i),* which heavily affects the chain composition along **a**, shows trends qualitatively in good agreement with the experimental.

Mechanisms *(ii)* and *(iii)* are not expected to influence the chains significantly as the difference in the ionic radii between Pb and Bi is only 0.16 Å. The **b** and **c** cell parameters, which represent the stacking direction of TMSO molecules and eventually interstitial iodide sites, are the one which undergoes significant variation in these cases. The experimentally determined lattice parameters (in black in Figure 5) indicate a substantial contraction of the a-axis with increasing Bi content. The calculated lattice parameters clearly show that only mechanism *(i)* can reproduce the correct contraction along a and not along the other axes. This corroborates mechanism *(i)* as the primary charge compensation mechanism after Bi insertion in the lattice, leading to solid solutions described by the stoichiometry $(TMSO)_3Pb_{3x}Bi_{2(1-x)}I_9$ ($0 \leq x \leq 1$).

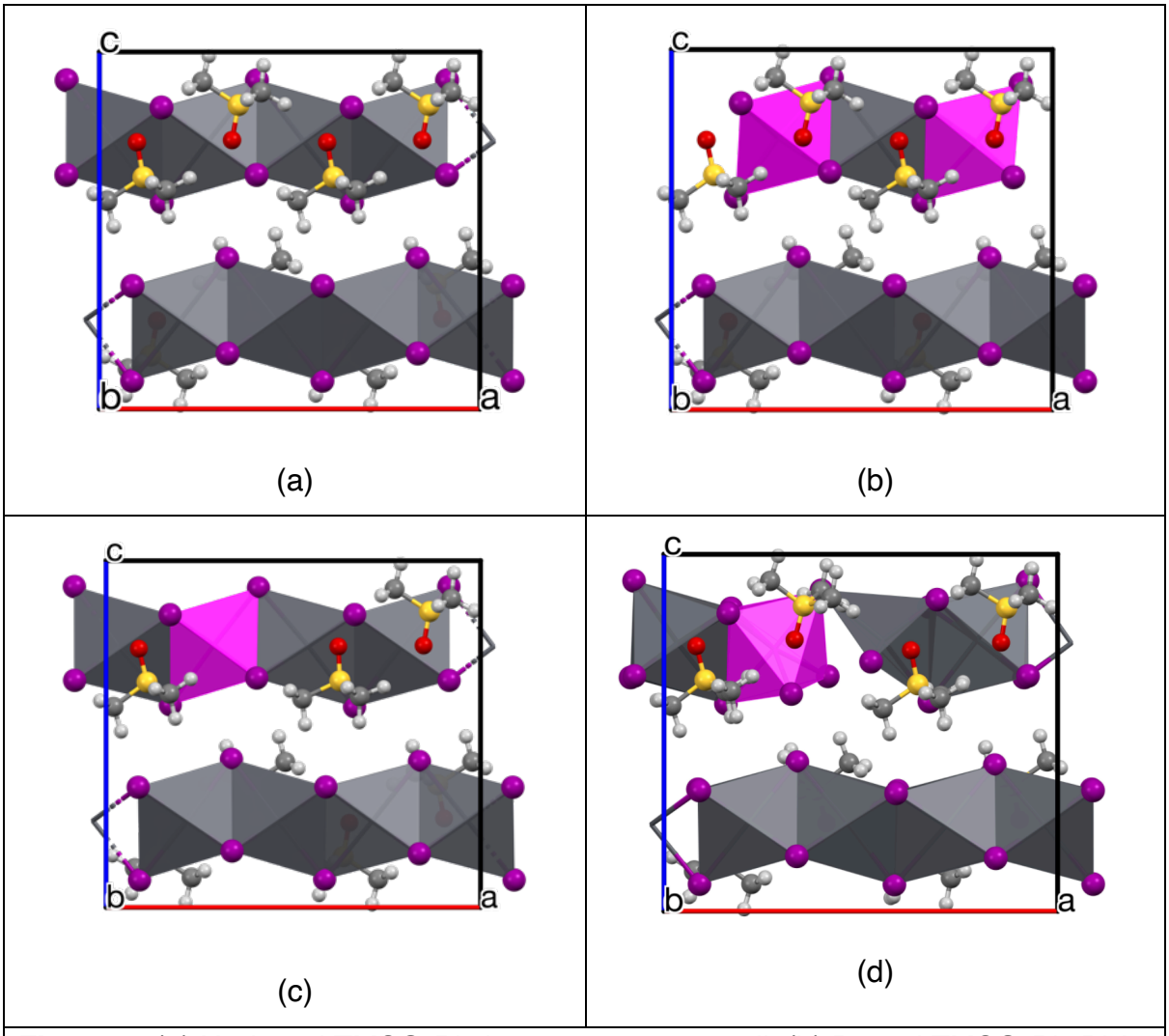

Figure 4. (a) Undoped $TMSO_8Pb_8I_{24}$ 2 x 1 x 1 supercell. (b) Doped $TMSO_8Pb_5Bi_2I_{24}$ supercell (Bi=25%). (c) Doped $TMSO_7Pb_7BiI_{24}$ supercell. (d) $TMSO_8Pb_7BiI_{25}$ (Bi=12.5%) supercell. Color code for atoms as in Figure 1, plus BiI_6 octahedra in pink.

Table 1. The binding energy for the neutral defect complexes.

Supercell	Defects	E_b (eV)
$(TMSO)_7Pb_8I_{23}$	$V_I^{\bullet} + V'_{TMSO}$	-2.04
$(TMSO)_8Pb_5Bi_2I_{24}$	$2Bi_{Pb}^{\bullet} + V''_{Pb}$	-4.62
$(TMSO)_7Pb_7BiI_{24}$	$Bi_{Pb}^{\bullet} + V'_{TMSO}$	-2.17
$(TMSO)_8Pb_7BiI_{25}$	$Bi_{Pb}^{\bullet} + I'_i$	-1.35

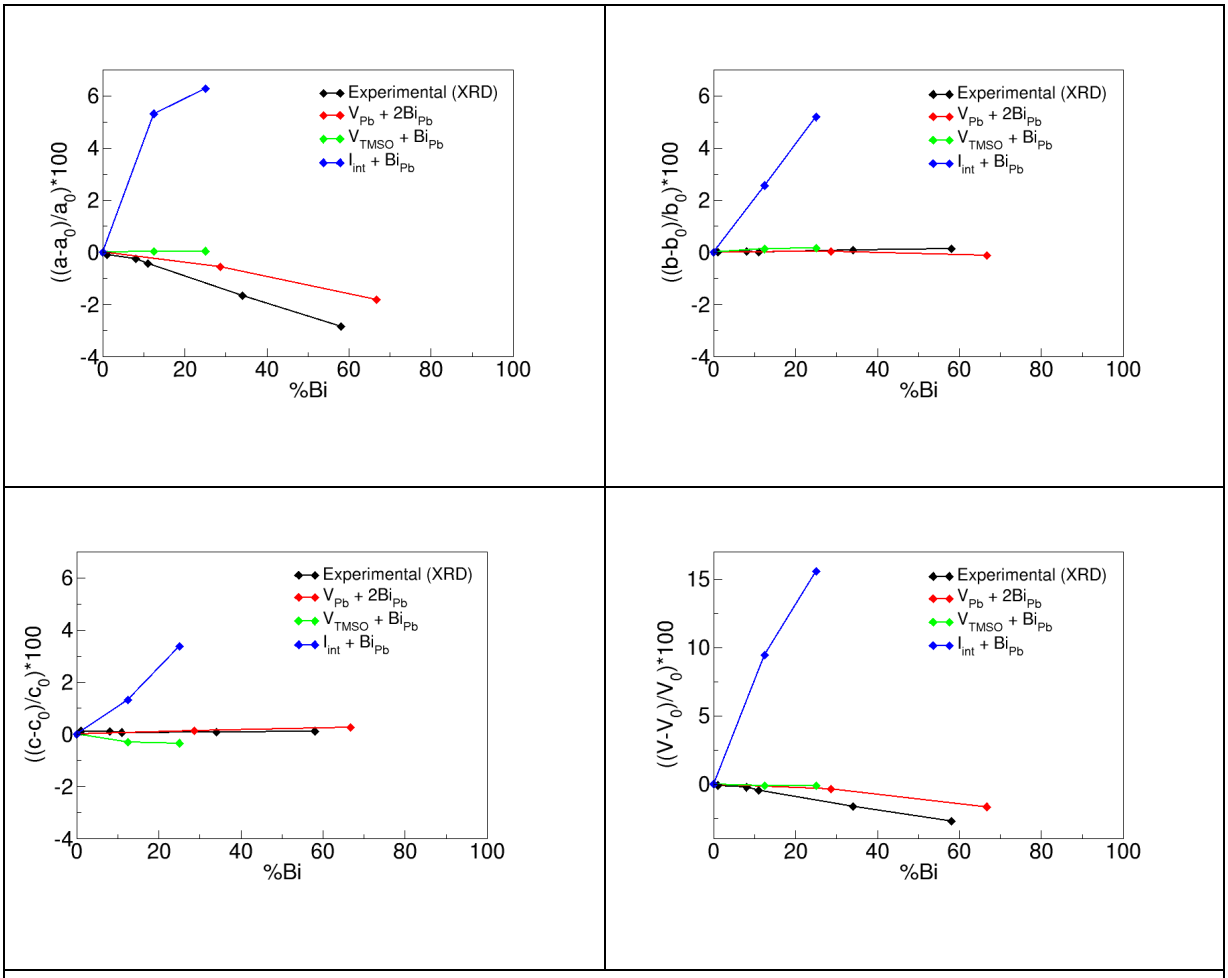

Figure 5. Cell parameters as a function of composition: experimental (black), and simulated for Pb vacancy compensation (red), TMSO vacancy compensation (green), and interstitial iodide compensation (blue). The relative scale is kept constant in the four panels to highlight the anisotropic lattice contraction as a function of doping.

The relaxed atomic positions of the $(TMSO)_8Pb_2Bi_4I_{24}$ supercell, containing two defect clusters $2Bi_{Pb}^{\bullet} + V_{Pb}''$, are in very good agreement with the experimentally determined Bi-I and Pb-I from X-ray absorption spectroscopy on $(TMSO)_3Pb_{0.99}Bi_{1.34}I_9$ (see Supporting Information). First and foremost, the EXAFS results unequivocally confirm Bi^{3+} ions substitute Pb^{2+} in a (slightly distorted) octahedral cavity.

Fittings are shown in Figure 6 and the Pb-I and Bi-I average distances and bond length variances are summarized in Table 2. It is worth noting that the high bond length variance (10^{-2} Å) arises from two different contributions: the one probed by DFT (at 0 K) represents only *static* disorder, coming from the different "frozen" bond lengths spread around the average. The experimentally probed disorder is both *static* and

thermal instead, as it also comes from vibrationally elongated and shortened bonds. It can be concluded that: the disorder in BiI_6 distorted octahedra is significant and essentially static in nature, arising from different Bi-I bonds; PbI_6 octahedra, on the contrary, are fairly regular, and their disorder is almost all vibrational. In any case, the difference between these kinds of disorders is lost at room temperature, and all metal-iodide correlations end up having a similar high variance. These results show no evidence of DY centers (negative defect complexes featuring a heavily distorted Bi environment and longer Bi-I bonds) described in MAPBr. [39]

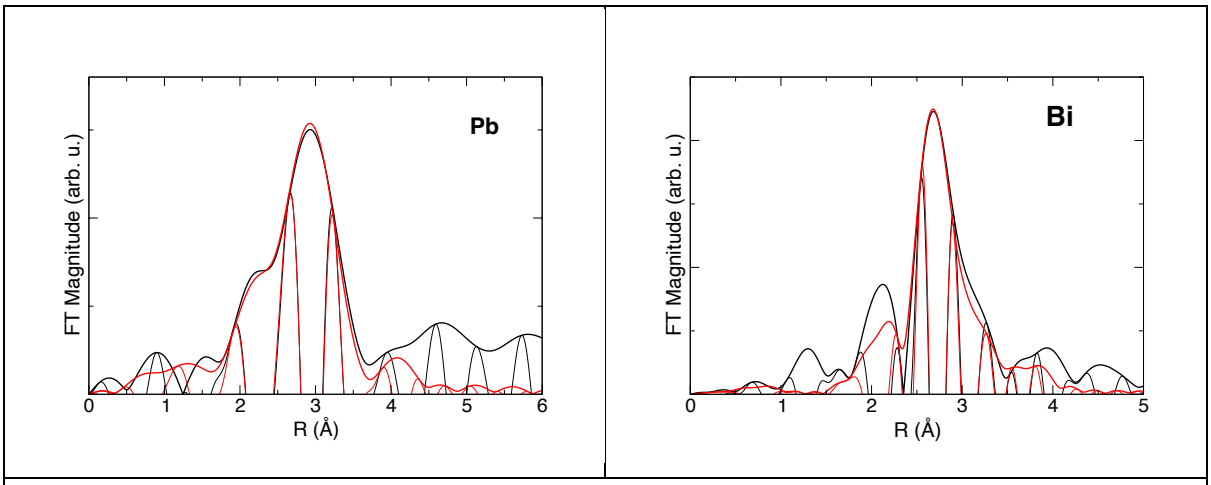

Figure 6 – Fourier-transformed EXAFS spectra (black) and best fit (red) at the Pb L_3-edge (left) and Bi L_3-edge (right).

Table 2. Local structure parameters from the relaxed structure and experimentally determined from X-ray absorption spectroscopy (EXAFS). Uncertainty in parentheses.

	R (Å)	**σ^2, (Å^2)**
Pb-I		
EXAFS	3.16(2)	0.02(1)
DFT	3.16	10^{-4}
Bi-I		
EXAFS	3.12(2)	0.03(1)
DFT	3.13	0.02

3.5. Interactions between metal cation sites: atomistic simulations

Figure 7 shows a schematic depiction of the local structure around a Pb site. Due to the linear arrangement of octahedra, in pristine undefective (TMSO)PbI_3, each Pb atom has two cation first neighbors at 3.9 Å (red dashes) and two cation second neighbors at 7.8 Å (blue dashes). Farther cation neighbors that reside in adjacent chains at around 9-10 Å and beyond are depicted in Figure S2.

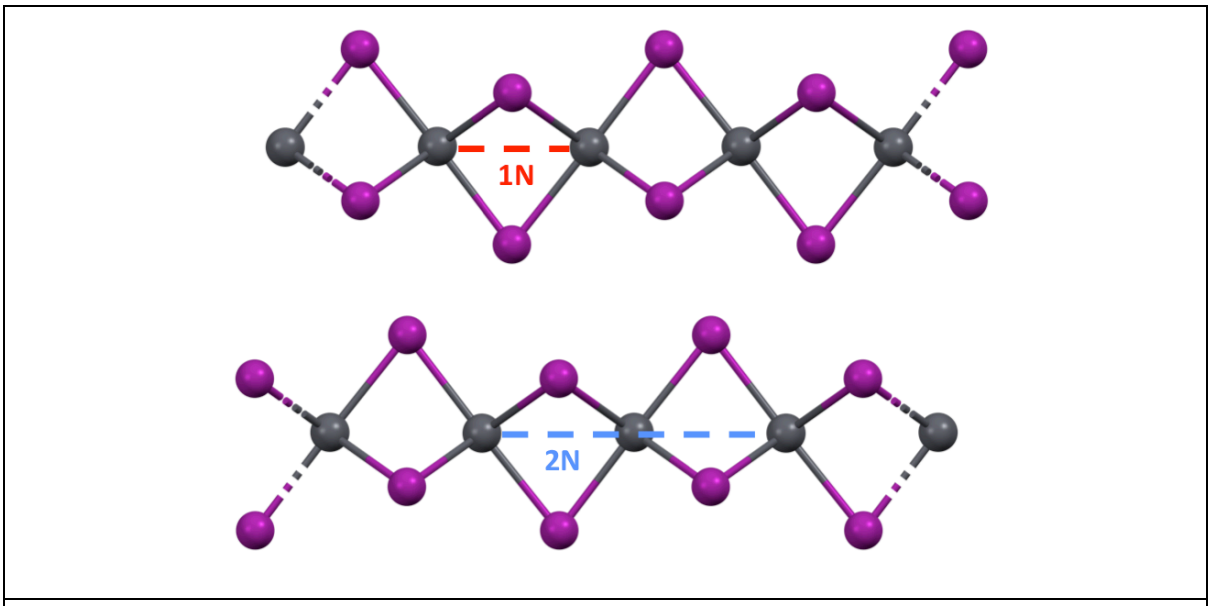

Figure 7. Cation-cation distances in (TMSO)PbI_3. The Pb-I chains are represented schematically as flat in this diagram to highlight the cation-cation pairs. The first and second neighbor distances are highlighted as red (1N) and blue (2N) dashes, respectively. The color code for atoms is in Figure 1.

Considering that the vacancy formation on the Pb site is the charge compensation mechanism after the insertion of Bi, we study the energetics of the system as a function of all possible atomic arrangements for the $2Bi_{Pb}^{\bullet} + V_{Pb}^{\prime\prime}$ defect complex in a 2x1x1 supercell. Such a supercell contains 8 cation sites occupied by 5 Pb^{2+}, 2 Bi^{3+}, and 1 vacancy, resulting in $(TMSO)_8Pb_5Bi_2I_{24}$ (x=0.62, Bi=28%). All different arrangments of Pb/Bi/V in the supercell resulted in 16 inequivalent configurations (described in full in the Supporting Information). Among all 16 possible defect configurations, five (A, B,

C, I, and P) features differ in their first-neighbor pairs and are depicted in Figure 8 and detailed in Table 3.

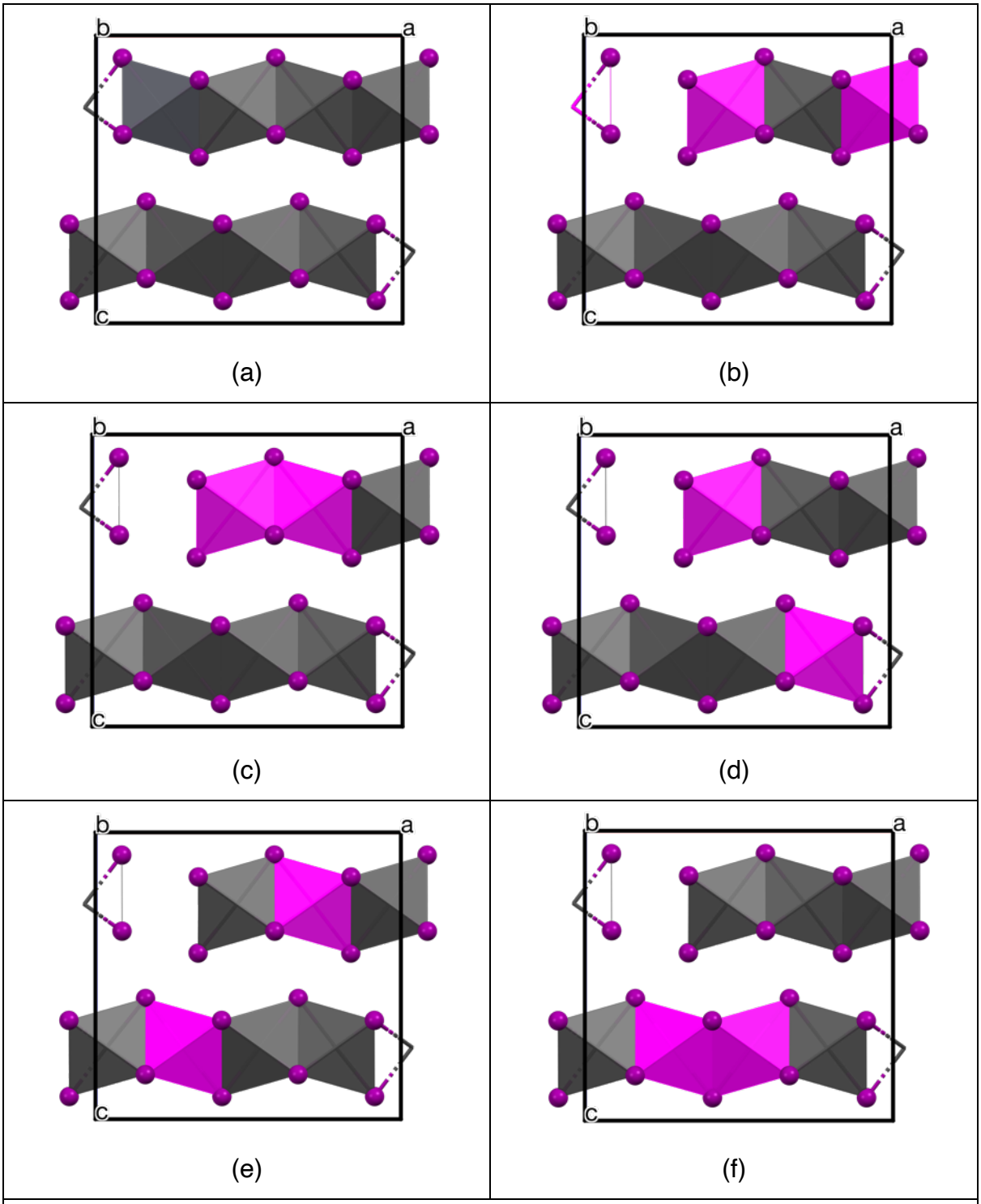

Figure 8. Configurations featuring different first neighbor pairs in $(TMSO)_8Pb_5Bi_2I_{24}$. Undoped sample (a), configuration A (b), configuration B (c), configuration C (d), configuration I (e) and configuration P (f).The PbI_6 octahedra are depicted in grey,

BiI_6 octahedra in magenta, and I atoms in violet. The color code for atoms is in Figure 1.

Table 3. The number of first-neighbor pairs in the configuration shown in Figure 7.

	Number of pairs				
Configuration	Pb-Pb	Bi-Bi	Pb-Bi	V-Bi	V-Pb
A	4	0	2	2	0
B	4	1	1	1	1
C	3	0	3	1	1
I	2	0	4	0	2
P	3	1	2	0	2

The effect of the cation placement inside a supercell has been recently used in oxide perovskites to explain the bandgap reduction as a function of the position of a dopant in the cation sublattice [40]. In the following, we apply a similar approach to explore the correlation between the energy of a configuration and the occurrence of B-site pairs and triads inside the 1D chains.

The total energy difference between two given configurations is only due to the different interaction energy terms between cation pairs, everything else (anions, TMSO ions) being equal. The relative energy of each structure is then factorized as:

$$E_{tot} = \sum E_{1N} + \sum E_{2N} + \sum E_{other} \qquad \textit{(Eq. x)}$$

Where E_{1N} represents the interaction energy due to each first-neighbor cation-cation pair (at 3.9 Å apart), and E_{2N} represents the interaction energy due to a second-neighbor cation-cation correlation (at 7.8 Å apart), as shown in Figure 7. E_{other} describes all farther cation-cation interactions between adjacent chains. These are neglected in the following discussion since each cation-cation interaction between adjacent chains is at least two orders of magnitude less important than between first neighbors (see Supporting Information for details). E_{1N} and E_{2N} contain five different terms each (i.e., Pb-Pb, Pb-Bi, Bi-Bi, Pb-V, and Bi-V) for the first and second-neighbor interactions; this results in ten additional energy terms being responsible for all calculated energy differences between configurations. As an example, the following equations show E_{tot} factorization for configurations A and B:

$E_{tot,A} = 4\ E_{1,Pb\text{-}Pb} + 2\ E_{1,Pb\text{-}Bi} + 2\ E_{1,V\text{-}Bi} + 4\ E_{2,Pb\text{-}Pb} + 2\ E_{2,Bi\text{-}Bi} + 2\ E_{2,V\text{-}Pb}$

$E_{tot,B} = 4\ E_{1,Pb\text{-}Pb} + 1\ E_{1,Bi\text{-}Bi} + 1\ E_{1,Pb\text{-}Bi} + 1\ E_{1,V\text{-}Bi} + 1\ E_{1,V\text{-}Pb} + 4\ E_{2,Pb\text{-}Pb} + 2\ E_{2,Pb\text{-}Bi} + 2\ E_{2,V\text{-}Bi}$

The DFT simulations give E_{tot}values for each A, B, … configuration (reported in the Supporting Information), resulting in a sparse and noisy linear system with ten unknowns (the energy terms described above).

The relative energy fluctuates by about 1.5 eV between the lowest and highest energy configurations, representing the order of magnitude of the energy due to cation placement. Comparing those configurations with the same first-neighbor cation correlations (E_{1N}), and that differ only for E_{2N} contributions (e.g., D and E), it can be seen that their energies differ by about 0.06-0.15 eV. As it is expected, E_{2N} has relatively lower importance in determining bond energy, and cation-cation first neighbor interactions dominate the total energy differences.

After solving the linear system described above, the ten energy contribution terms due to each Pb-Pb, Pb-Bi, etc., can be derived (shown in Table 4). These represent the relative energy of each M-M first neighbor or second neighbor pair occurring in the structure.

Table 4. Energy contributions (in eV) of different first and second neighbor pairs. X represents any possible cation site. Uncertainty is on the last significant digit.

First Neighbor	E_{1N}(eV)	Second Neighbor	E_{2N} (eV)
Pb-Pb	0.073	Pb-X-Pb	-0.03
Bi-Bi	0.33	Bi-X-Bi	0.1
Pb-Bi	0.054	Pb-X-Bi	-0.002
Bi-V	-0.27	Bi-X-V	-0.04
Pb-V	0.435	Pb-X-V	0.03

As a validation of the robustness of such an approach, the pair contributions to energy E_{1N} and E_{2N} reported in Table 3 can be used to re-calculate the energy of all 16 possible configurations and compare these with the values obtained with DFT. This procedure yields values that are self-consistent down to a 0.05 eV accuracy.

A few interesting considerations can then be summarized from inspection of Table 4: a) the most relevant energy costs are due to Pb-V pairs and Bi-Bi clusterization; b) Bi-V pairs, on the contrary, are energetically favored (it is the only pairs with the negative sign); c) the clusterization of Pb-Pb is the most likely consequence, segregating (Bi/V)-rich regions to avoid Pb-V pairs; d) interactions between second neighbors are in general significantly lower with respect to the first neighbors, but not negligible, especially for Bi-Bi pairs, providing an observable basis for the second-order Markov chain analysis.

The stochastic matrix elements can then be calculated for every non-equivalent configuration of defects in $(TMSO)_8Pb_5Bi_2I_{24}$. The lowest-energy configurations have large matrix elements for V-Bi → Pb, Pb-V → Bi and Bi-V → Pb; on the contrary, large matrix elements Bi-Bi → Pb, Pb-Bi → Bi and Pb-V → Pb are all associated with the highest-energy configurations.

Further validation of the energy contributions of Table 4 was carried out on a 2x1x1 supercell with a higher Bi content, $(TMSO)_8Pb_2Bi_4I_{24}$ (x=0.25, Bi=75%), to investigate the possibility to extend these energy terms also on a different composition. A $(TMSO)_8Pb_2Bi_4I_{24}$ 2x1x1 supercell contains one defect complex $4Bi_{Pb}^{\bullet} + 2V_{Pb}''$, which can be arranged within the 8 B sites. We then compared the total calculated DFT energy of four different configurations, labeled AB to AF, all having very different first neighbor arrangements; for consistency, the energy is reported relative to configuration A of $(TMSO)_8Pb_5Bi_2I_{24}$ and corrected for composition by suitable addition of chemical potentials. These energy values were compared to those calculated by applying equation 19, all reported in Table 5. They show a remarkable correlation, with a linear slope of 1.1. Such a chemical transferability between very distant compositions (i.e. $(TMSO)_8Pb_5Bi_2I_{24}$ and $(TMSO)_8Pb_2Bi_4I_{24}$) shows that the approach described above is robust and describes satisfactorily realistic solid solutions with a tunable concentration of interacting point defects in a wide range.

Table 5. The relative energy of selected configurations of $(TMSO)_8Pb_2Bi_4I_{24}$ derived using Equation 19 and Table 4 or calculated ab initio with periodic DFT.

Configuration	Expected E_{tot} from equation 19 (eV)	Calculated E_{tot} from DFT(eV)

AB	-0.28	-0.34
AC	0.44	0.59
AE	0.91	0.93
AF	0.93	1.08

3.6. Effect of Bi doping on the density of states

The substitution of lead with bismuth causes a significant reduction of the optical band gap as observed by UV/vis spectroscopy (in particular, a 0.54 eV reduction for $(TMSO)_3Pb_{2.67}Bi_{0.22}I_9$ compared to the undoped sample). [19] As shown in Figure 9, the Bi-I states at the CBM band lay around 1 eV lower than the corresponding Pb-I states (in A configuration). In addition, the latter are also split due to the inequivalent Pb sites (closer or farther away from defect sites) arising in the structure. The effect of the different configurations on DOS, and thus on predicted bandgap, is considerable. As reported in Figure 10, other configurations have Bi-I states at different energies, thus reducing the bandgap in different ways. Such a difference between experimental and predicted bandgap arises from the different chemical environments for the lead and bismuth, which split and spread throughout the bandgap the Bi-I and Pb-I states. Configurations A, M, and N all feature equivalent local environments for the two bismuth atoms in the structure and two different local environments for the lead atoms: both effects limit the splitting between the electronic levels. In particular, configuration A features the same local environment for both Bi sites, limiting the energy spread of Bi-I levels in the bandgap, resulting in the best agreement between the experimental (0.54 eV) and modeled (0.4 eV) bandgap reduction upon doping. These results leave room to explore the engineering of the bandgap of doped $TMSOPbI_3$ by developing a synthetic tool to control Bi^{3+} position in the lattice: different configurations can lead to different bandgap values. Moreover, Bi-I states belonging to Bi sites with the same first neighbors have similar, but not identical, energy positions (e.g. configuration G). The second neighbors may therefore also be important in determining the states close to the Fermi level. Thus, it is possible to control the bandgap of the material from wide to very low (e.g., in configurations M and N) and then to control the relevant technological properties of the perovskites, e.g., power conversion efficiency [41].

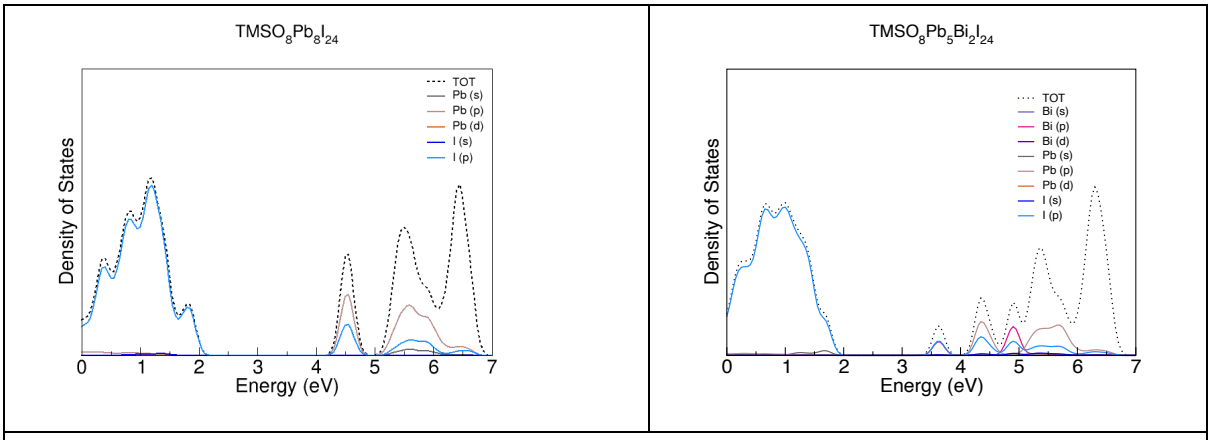

Figure 9. DOS of undoped $(TMSO)_8Pb_8I_{24}$ (left) and $(TMSO)_8Pb_5Bi_2I_{24}$ in configuration A (right). The contributions from lighter atoms are omitted for clarity.

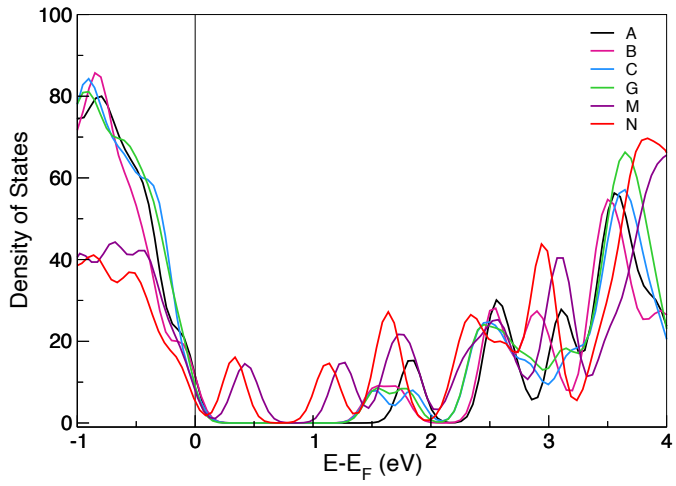

(a)

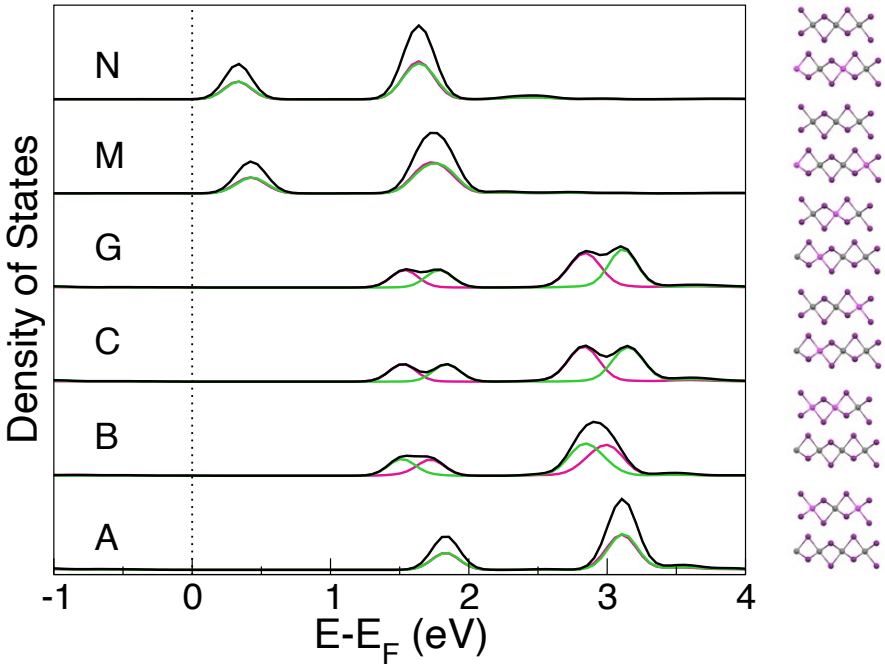

(b)

Figure 10. The density of states in A, B, C, G, M, and N configurations of $(TMSO)_8Pb_5Bi_2I_{24}$. (a) Total DOS. (b) PDOS of the Bi 6p states (black). The contributions of the two Bi atoms in the structure (depicted on the right) are shown separately with pink and green lines.

4. Conclusion

Bismuth doping is currently considered one of the promising routes to fine-tune the electronic properties of lead halide perovskites. We recently described the hybrid $(TMSO)_3Pb_{3x}Bi_{2(1-x)}I_9$ solid solutions with a monodimensional structure, where the presence of bismuth decreases the optical bandgap even at very low concentrations. [19] In this work, we combine evidence from DFT calculations and X-ray absorption spectroscopy to prove that positively charged Bi^{3+} defects are compensated by Pb^{2+} vacancies (as predicted for both $MAPbBr_3$ [42] and $CsPbBr_3$ [14]). The formation energy of point defects was calculated at the GGA-PBE level of theory. At the same time, binding energies were also used to evaluate the neutral cluster of defects, which take into account different charge compensation mechanisms. The most energetically favored is the $2Bi_{Pb}^{\bullet} + V_{Pb}''$ neutral defect complex, confirming previous hypotheses. [19] Atomistic simulations were also carried out to evaluate the differences for placing $Bi_{Pb}^{\bullet}$

and V''_{Pb} in supercells, showing that the point defects are preferentially clustered in Bi-V-Bi arrangements in the linear metal halide chains at high Bi concentrations. Therefore, the metal cation sublattice of $(TMSO)_3Pb_{3x}Bi_{2(1-x)}I_9$ deviates from the ideal solution model, in which competing sites are randomly distributed because of clustering of point defects. In turn, this results in the very peculiar X-ray diffraction peaks with a trapezoidal shape observed at high Bi concentrations (e.g. $(TMSO)_3Pb_{0.99}Bi_{1.34}I_9$). We used this hybrid pseudo-perovskites as a case study for its wide compositional range. Still, the same approach can be easily extended to other systems as inorganic or hybrid (pseudo-)perovskites where a similar interaction between defects needs to be taken into account at moderate dopant concentrations (e.g., 10%).

The introduction of Bi^{3+} in $(TMSO)PbI_3$ induces the appearance of several donor-acceptor defects in the region immediately below the conduction band, pinning the Fermi level to an n-type semiconductor. Moreover, it causes localized states below the conduction band, observed as lowered bandgaps in optical absorption experiments. We demonstrate that the effects of the position of the Bi^{3+} dopant in the lattice are essential for accurate bandgap prediction. Moreover, analysis of the different configurations highlights the possibility of modulating the bandgap of this doped material by engineering the Bi^{3+} position. Atomic-level engineering of short-range order could have significant consequences for application since it enables to control doped samples with a bandgap range spanning more than 1 eV.

This approach is expected to shed light on the defect interactions in this class of doped materials and devise strategies to correlate the local structure of the dopants with the electronic structure close to the bandgap. The deeper knowledge of the electronic structure has implications for the engineering of doped materials, which find vast applications in optoelectronic devices.

Conflicts of interest

The authors declare no competing financial interest.

ACKNOWLEDGMENTS

This project was partially supported by MIUR (PRIN-2017L8WW48, Project HY-TEC) and the University of Padova (grant: P-DISC #CARL-SID17 BIRD2017-UNIPD, project CHIRoN). We acknowledge the CINECA award under the ISCRA initiative for the availability of high-performance computing resources and support (project IsC83_1HyPe). The staff of beamline BM8 at ESRF and the Computational Chemistry Community (C_3P) of the University of Padova are kindly acknowledged.

REFERENCES

(1) Zhao, Y.; Zhu, K. Organic–Inorganic Hybrid Lead Halide Perovskites for Optoelectronic and Electronic Applications. *Chem. Soc. Rev.* **2016**, *45*, 655–689. https://doi.org/10.1039/C4CS00458B.

(2) Chen, Q.; De Marco, N.; Yang, Y. (Michael); Song, T.-B.; Chen, C.-C.; Zhao, H.; Hong, Z.; Zhou, H.; Yang, Y. Under the Spotlight: The Organic–Inorganic Hybrid Halide Perovskite for Optoelectronic Applications. *Nano Today* **2015**, *10*, 355–396. https://doi.org/10.1016/j.nantod.2015.04.009.

(3) Biswas, A.; Bakthavatsalam, R.; Shaikh, S. R.; Shinde, A.; Lohar, A.; Jena, S.; Gonnade, R. G.; Kundu, J. Efficient Broad-Band Emission from Contorted Purely Corner-Shared One Dimensional (1D) Organic Lead Halide Perovskite. *Chem. Mater.* **2019**, *31*, 2253–2257. https://doi.org/10.1021/acs.chemmater.9b00069.

(4) Kamminga, M. E.; de Wijs, G. A.; Havenith, R. W. A.; Blake, G. R.; Palstra, T. T. M. The Role of Connectivity on Electronic Properties of Lead Iodide Perovskite-Derived Compounds. *Inorg. Chem.* **2017**, *56*, 8408–8414. https://doi.org/10.1021/acs.inorgchem.7b01096.

(5) Mao, L.; Stoumpos, C. C.; Kanatzidis, M. G. Two-Dimensional Hybrid Halide Perovskites: Principles and Promises. *J. Am. Chem. Soc.* **2019**, *141*, 1171–1190. https://doi.org/10.1021/jacs.8b10851.

(6) Akkerman, Q. A.; Manna, L. What Defines a Halide Perovskite? *ACS Energy Lett.* **2020**, *5*, 604–610. https://doi.org/10.1021/acsenergylett.0c00039.

(7) Meggiolaro, D.; De Angelis, F. First-Principles Modeling of Defects in Lead Halide Perovskites: Best Practices and Open Issues. *ACS Energy Lett.* **2018**, *3*, 2206–2222. https://doi.org/10.1021/acsenergylett.8b01212.

(8) Euvrard, J.; Yan, Y.; Mitzi, D. B. Electrical Doping in Halide Perovskites. *Nat Rev Mater* **2021**, *6*, 531–549. https://doi.org/10.1038/s41578-021-00286-z.

(9) Zhang, X.; Li, L.; Sun, Z.; Luo, J. Rational Chemical Doping of Metal Halide Perovskites. *Chem. Soc. Rev.* **2019**, *48*, 517–539. https://doi.org/10.1039/C8CS00563J.

(10) Zhang, X.; Shen, J.-X.; Turiansky, M. E.; Van de Walle, C. G. Hidden Role of Bi Incorporation in Nonradiative Recombination in Methylammonium Lead Iodide. *J. Mater. Chem. A* **2020**, *8*, 12964–12967. https://doi.org/10.1039/D0TA04968A.

(11) Yin, J.; Ahmed, G. H.; Bakr, O. M.; Brédas, J.-L.; Mohammed, O. F. Unlocking the Effect of Trivalent Metal Doping in All-Inorganic $CsPbBr_3$ Perovskite. *ACS Energy Lett.* **2019**, *4*, 789–795. https://doi.org/10.1021/acsenergylett.9b00209.

(12) Kang, Y.; Kang, S.; Han, S. Influence of Bi Doping on Physical Properties of Lead Halide Perovskites: A Comparative First-Principles Study between $CsPbI_3$ and $CsPbBr_3$. *Mater. Today Adv.* **2019**, *3*, 100019. https://doi.org/10.1016/j.mtadv.2019.100019.

(13) Jedlicka, E.; Wang, J.; Mutch, J.; Jung, Y.-K.; Went, P.; Mohammed, J.; Ziffer, M.; Giridharagopal, R.; Walsh, A.; Chu, J.-H.; Ginger, D. S. Bismuth Doping Alters Structural Phase Transitions in Methylammonium Lead Tribromide Single Crystals. *J. Phys. Chem. Lett.* **2021**, *12*, 2749–2755. https://doi.org/10.1021/acs.jpclett.1c00334.

(14) Lyons, J. L. Effective Donor Dopants for Lead Halide Perovskites. *Chem. Mater.* **2021**, *33*, 6200–6205. https://doi.org/10.1021/acs.chemmater.1c01898.

(15) Rakita, Y.; Lubomirsky, I.; Cahen, D. When Defects Become 'Dynamic': Halide Perovskites: A New Window on Materials? *Mater. Horiz.* **2019**, *6*, 1297–1305. https://doi.org/10.1039/C9MH00606K.

(16) Mosconi, E.; Merabet, B.; Meggiolaro, D.; Zaoui, A.; De Angelis, F. First-Principles Modeling of Bismuth Doping in the $MAPbI_3$ Perovskite. *J. Phys. Chem. C* **2018**, *122*, 14107–14112. https://doi.org/10.1021/acs.jpcc.8b01307.

(17) Leguy, A. M. A.; Hu, Y.; Campoy-Quiles, M.; Alonso, M. I.; Weber, O. J.; Azarhoosh, P.; van Schilfgaarde, M.; Weller, M. T.; Bein, T.; Nelson, J.; Docampo, P.; Barnes, P. R. F. Reversible Hydration of $CH_3NH_3PbI_3$ in Films,

Single Crystals, and Solar Cells. *Chem. Mater.* **2015**, *27*, 3397–3407. https://doi.org/10.1021/acs.chemmater.5b00660.

(18) Parashar, M.; Singh, R.; Yoo, K.; Lee, J.-J. Formation of 1-D/3-D Fused Perovskite for Efficient and Moisture Stable Solar Cells. *ACS Appl. Energy Mater.* **2021**, *4* (3), 2751–2760. https://doi.org/10.1021/acsaem.1c00028.

(19) Pipitone, C.; Giannici, F.; Martorana, A.; García-Espejo, G.; Carlotto, S.; Casarin, M.; Guagliardi, A.; Masciocchi, N. Heterovalent Bi ^{III} /Pb ^{II} Ionic Substitution in One-Dimensional Trimethylsulfoxonium Halide Pseudo-Perovskites (X = I, Br). *J. Phys. Chem. C* **2021**, *125*, 11728–11742. https://doi.org/10.1021/acs.jpcc.1c02571.

(20) Giannozzi, P.; Baseggio, O.; Bonfà, P.; Brunato, D.; Car, R.; Carnimeo, I.; Cavazzoni, C.; de Gironcoli, S.; Delugas, P.; Ferrari Ruffino, F.; Ferretti, A.; Marzari, N.; Timrov, I.; Urru, A.; Baroni, S. QUANTUM ESPRESSO toward the Exascale. *J. Chem. Phys.* **2020**, *152*, 154105. https://doi.org/10.1063/5.0005082.

(21) Giannozzi, P.; Baroni, S.; Bonini, N.; Calandra, M.; Car, R.; Cavazzoni, C.; Ceresoli, D.; Chiarotti, G. L.; Cococcioni, M.; Dabo, I.; Dal Corso, A.; de Gironcoli, S.; Fabris, S.; Fratesi, G.; Gebauer, R.; Gerstmann, U.; Gougoussis, C.; Kokalj, A.; Lazzeri, M.; Martin-Samos, L.; Marzari, N.; Mauri, F.; Mazzarello, R.; Paolini, S.; Pasquarello, A.; Paulatto, L.; Sbraccia, C.; Scandolo, S.; Sclauzero, G.; Seitsonen, A. P.; Smogunov, A.; Umari, P.; Wentzcovitch, R. M. QUANTUM ESPRESSO: A Modular and Open-Source Software Project for Quantum Simulations of Materials. *J. Phys.: Condens. Matter* **2009**, *21*, 395502. https://doi.org/10.1088/0953-8984/21/39/395502.

(22) Giannozzi, P.; Andreussi, O.; Brumme, T.; Bunau, O.; Buongiorno Nardelli, M.; Calandra, M.; Car, R.; Cavazzoni, C.; Ceresoli, D.; Cococcioni, M.; Colonna, N.; Carnimeo, I.; Dal Corso, A.; de Gironcoli, S.; Delugas, P.; DiStasio, R. A.; Ferretti, A.; Floris, A.; Fratesi, G.; Fugallo, G.; Gebauer, R.; Gerstmann, U.; Giustino, F.; Gorni, T.; Jia, J.; Kawamura, M.; Ko, H.-Y.; Kokalj, A.; Küçükbenli, E.; Lazzeri, M.; Marsili, M.; Marzari, N.; Mauri, F.; Nguyen, N. L.; Nguyen, H.-V.; Otero-de-la-Roza, A.; Paulatto, L.; Poncé, S.; Rocca, D.; Sabatini, R.; Santra, B.; Schlipf, M.; Seitsonen, A. P.; Smogunov, A.; Timrov, I.; Thonhauser, T.;

Umari, P.; Vast, N.; Wu, X.; Baroni, S. Advanced Capabilities for Materials Modelling with Quantum ESPRESSO. *J. Phys.: Condens. Matter* **2017**, *29*, 465901. https://doi.org/10.1088/1361-648X/aa8f79.

(23) Anisimov, V. I.; Zaanen, J.; Andersen, O. K. Band Theory and Mott Insulators: Hubbard *U* Instead of Stoner *I*. *Phys. Rev. B* **1991**, *44*, 943–954. https://doi.org/10.1103/PhysRevB.44.943.

(24) Perdew, J. P.; Burke, K.; Ernzerhof, M. Generalized Gradient Approximation Made Simple. *Phys. Rev. Lett.* **1996**, *77*, 3865–3868. https://doi.org/10.1103/PhysRevLett.77.3865.

(25) Blöchl, P. E. Projector Augmented-Wave Method. *Phys. Rev. B* **1994**, *50*, 17953–17979. https://doi.org/10.1103/PhysRevB.50.17953.

(26) Naik, M. H.; Jain, M. CoFFEE: Corrections For Formation Energy and Eigenvalues for Charged Defect Simulations. *Comput. Phys. Commun.* **2018**, *226*, 114–126. https://doi.org/10.1016/j.cpc.2018.01.011.

(27) Klementev, K. V. Extraction of the Fine Structure from X-Ray Absorption Spectra. *J. Phys. D: Appl. Phys.* **2001**, *34*, 209–217. https://doi.org/10.1088/0022-3727/34/2/309.

(28) Freysoldt, C.; Neugebauer, J.; Van de Walle, C. G. Fully *Ab Initio* Finite-Size Corrections for Charged-Defect Supercell Calculations. *Phys. Rev. Lett.* **2009**, *102*, 016402. https://doi.org/10.1103/PhysRevLett.102.016402.

(29) Makov, G.; Payne, M. C. Periodic Boundary Conditions in *Ab Initio* Calculations. *Phys. Rev. B* **1995**, *51* (7), 4014–4022. https://doi.org/10.1103/PhysRevB.51.4014.

(30) Lany, S.; Zunger, A. Assessment of Correction Methods for the Band-Gap Problem and for Finite-Size Effects in Supercell Defect Calculations: Case Studies for ZnO and GaAs. *Phys. Rev. B* **2008**, *78*, 235104. https://doi.org/10.1103/PhysRevB.78.235104.

(31) Goyal, A.; Mathew, K.; Hennig, R. G.; Chernatynskiy, A.; Stanek, C. R.; Murphy, S. T.; Andersson, D. A.; Phillpot, S. R.; Uberuaga, B. P. The Conundrum of Relaxation Volumes in First-Principles Calculations of Charged Defects in UO2. *Applied Sciences* **2019**, *9* (24), 5276. https://doi.org/10.3390/app9245276.

(32) Castleton, C. W. M.; Höglund, A.; Mirbt, S. Density Functional Theory Calculations of Defect Energies Using Supercells. *Modelling Simul. Mater. Sci. Eng.* **2009**, *17*, 084003. https://doi.org/10.1088/0965-0393/17/8/084003.

(33) Barboni, D.; De Souza, R. A. The Thermodynamics and Kinetics of Iodine Vacancies in the Hybrid Perovskite Methylammonium Lead Iodide. *Energy Environ. Sci.* **2018**, *11*, 3266–3274. https://doi.org/10.1039/C8EE01697F.

(34) Chen, X.; Cheng, S.; Xiao, L.; Sun, H. Identifying, Understanding and Controlling Defects and Traps in Halide Perovskites for Optoelectronic Devices: A Review. *J. Phys. D: Appl. Phys.* **2020**, *53*, 373001. https://doi.org/10.1088/1361-6463/ab9134.

(35) Yuan, Y.; Chae, J.; Shao, Y.; Wang, Q.; Xiao, Z.; Centrone, A.; Huang, J. Photovoltaic Switching Mechanism in Lateral Structure Hybrid Perovskite Solar Cells. *Adv. Energy Mater.* **2015**, *5*, 1500615. https://doi.org/10.1002/aenm.201500615.

(36) Deng, Y.; Xiao, Z.; Huang, J. Light-Induced Self-Poling Effect on Organometal Trihalide Perovskite Solar Cells for Increased Device Efficiency and Stability. *Adv. Energy Mater.* **2015**, *5*, 1500721. https://doi.org/10.1002/aenm.201500721.

(37) Whitmire, K. H. Bismuth: Inorganic Chemistry. In *Encyclopedia of Inorganic and Bioinorganic Chemistry*; Scott, R. A., Ed.; John Wiley & Sons, Ltd: Chichester, UK, 2004; pp 1–32. https://doi.org/10.1002/9781119951438.eibc0018.pub2.

(38) Walsh, A.; Scanlon, D. O.; Chen, S.; Gong, X. G.; Wei, S. Self-Regulation Mechanism for Charged Point Defects in Hybrid Halide Perovskites. *Angew. Chem.* **2015**, *127*, 1811–1814. https://doi.org/10.1002/ange.201409740.

(39) Li, J.-L.; Yang, J.; Wu, T.; Wei, S.-H. Formation of DY Center as N-Type Limiting Defects in Octahedral Semiconductors: The Case of Bi-Doped Hybrid Halide Perovskites. *J. Mater. Chem. C* **2019**, *7*, 4230–4234. https://doi.org/10.1039/C8TC06222F.

(40) Seyfouri, M. M.; Liu, Q.; Yang, J.; Sun, Y.; Dai, X.; Shi, J.; Tan, X.; Li, S.; Wu, T.; Wang, D. New Insights on the Substantially Reduced Bandgap of Bismuth Layered Perovskite Oxide Thin Films. *J. Mater. Chem. C* **2021**, *9*, 3161–3170. https://doi.org/10.1039/D0TC05300G.

(41) Yang, R.; Li, R.; Cao, Y.; Wei, Y.; Miao, Y.; Tan, W. L.; Jiao, X.; Chen, H.; Zhang, L.; Chen, Q.; Zhang, H.; Zou, W.; Wang, Y.; Yang, M.; Yi, C.; Wang, N.; Gao, F.; McNeill, C. R.; Qin, T.; Wang, J.; Huang, W. Oriented Quasi-2D Perovskites for High Performance Optoelectronic Devices. *Adv. Mater.* **2018**, *30*, 1804771. https://doi.org/10.1002/adma.201804771.

(42) Mannodi-Kanakkithodi, A.; Park, J.-S.; Jeon, N.; Cao, D. H.; Gosztola, D. J.; Martinson, A. B. F.; Chan, M. K. Y. Comprehensive Computational Study of Partial Lead Substitution in Methylammonium Lead Bromide. *Chem. Mater.* **2019**, *31*, 3599–3612. https://doi.org/10.1021/acs.chemmater.8b04017.